

High-Level Fault-Tolerant Abstractions for Quantum-Gate Circuit Design and Synthesis: PQC and Topological Anyon Architectures (TQC) for Categorical Computations in $SU(2)_3$ TQFT and D-brane Stability

Vaidik A Sharma*, Sainath Bitragunta

Department of Electrical & Electronics Engineering

Birla Institute of Technology and Science Pilani

*Email: f20212509@pilani.bits-pilani.ac.in

Abstract—We propose a dual-architecture quantum simulation framework for modeling morphisms and stability conditions in the bounded derived category $D^b(\text{Coh}(X))$, with applications to D-brane physics on Kähler and non-Kähler manifolds. Two physically executable quantum realizations are constructed: parameterized quantum circuits (PQCs) implemented on conventional gate-based qubit platforms, and a topological quantum computing (TQC) realization using braiding and fusion of Fibonacci anyons modeled via $SU(2)_3$ modular tensor categories. In the PQC model, we encode slope functionals $S(\mathcal{F})$ and stability constraints as variational observables, mapping derived morphisms to unitaries that evolve over parameterized angles. The output expectation values simulate quantum-corrected Chern class inequalities with deformation terms δ , capturing quantum corrections to classical geometric stability. In the TQC model, we engineer braid group representations to implement functorial transformations such as spherical twists and autoequivalences as sequences of fault-tolerant braid operations. This bifurcated approach provides a robust engineering pipeline for simulating categorical stability and homological algebra on quantum hardware, bridging abstract derived category theory with executable quantum architectures.

I. INTRODUCTION

D-branes are fundamental objects in string theory, and their study on non-Kähler manifolds presents unique challenges and opportunities for mathematical exploration. In this section, we will derive novel stability conditions for coherent sheaves associated with D-branes, constructing a mathematical framework that bridges the gap between classical and noncommutative geometries.

We begin by defining the stability conditions for coherent sheaves on a non-Kähler manifold X and then rigorously derive new stability conditions using tools from derived categories.

II. MATHEMATICAL FRAMEWORK

Let X be a smooth complex manifold, and let $\text{Coh}(X)$ denote the category of coherent sheaves on X . The derived category $D^b(\text{Coh}(X))$ consists of bounded complexes of coherent sheaves:

$$\mathcal{K}^\bullet : \cdots \rightarrow \mathcal{K}^n \rightarrow \mathcal{K}^{n+1} \rightarrow \mathcal{K}^{n+2} \rightarrow \cdots,$$

with morphisms defined up to homotopy. For any coherent sheaf \mathcal{F} , we define the slope function as:

$$\mu(\mathcal{F}) = \frac{c_1(\mathcal{F})}{\text{rk}(\mathcal{F})},$$

where $c_1(\mathcal{F})$ is the first Chern class of the sheaf, and $\text{rk}(\mathcal{F})$ is its rank.

A. Novel Stability Condition

We propose a novel stability condition defined as follows:

$$S(\mathcal{F}) = \begin{cases} 1 & \text{if } \mu(\mathcal{F}) > 0, \\ 0 & \text{if } \mu(\mathcal{F}) = 0, \\ -1 & \text{if } \mu(\mathcal{F}) < 0. \end{cases}$$

This stability condition is motivated by physical considerations of D-brane stability and the requirement for coherent sheaves to support nontrivial gauge theories.

III. PROOF OF NOVEL STABILITY CONDITION

We will now prove that the proposed stability condition $S(\mathcal{F})$ is consistent under the derived category framework.

A. Step 1: Slope Function Properties

First, we will show that the slope function $\mu(\mathcal{F})$ retains the following properties:

1. Positivity: If \mathcal{F} is a stable sheaf, then $\mu(\mathcal{F}) > 0$.
2. Vanishing: If \mathcal{F} is a strictly semistable sheaf, then $\mu(\mathcal{F}) = 0$.
3. Negativity: If \mathcal{F} is an unstable sheaf, then $\mu(\mathcal{F}) < 0$.

1) *Proof of Positivity:* Let \mathcal{F} be a stable sheaf. By definition, any nontrivial sub-sheaf $\mathcal{G} \subset \mathcal{F}$ must satisfy:

$$\mu(\mathcal{G}) < \mu(\mathcal{F}).$$

Assume for contradiction that $\mu(\mathcal{F}) \leq 0$. This implies $\mu(\mathcal{G}) \leq 0$ for all \mathcal{G} , leading to a contradiction. Thus, we conclude $\mu(\mathcal{F}) > 0$.

2) *Proof of Vanishing:* Assume \mathcal{F} is strictly semistable. For any nontrivial sub-sheaf $\mathcal{G} \subset \mathcal{F}$, we have $\mu(\mathcal{G}) \leq \mu(\mathcal{F})$. If $\mu(\mathcal{F}) < 0$, then we reach a contradiction as before. Hence, $\mu(\mathcal{F}) = 0$.

3) *Proof of Negativity:* Now, let \mathcal{F} be an unstable sheaf. By definition, there exists a nontrivial sub-sheaf $\mathcal{G} \subset \mathcal{F}$ such that:

$$\mu(\mathcal{G}) \geq \mu(\mathcal{F}).$$

Assuming $\mu(\mathcal{F}) \geq 0$ leads to a contradiction. Thus, we find $\mu(\mathcal{F}) < 0$.

B. Step 2: Stability Condition Consistency

Now we must show that our proposed stability condition $S(\mathcal{F})$ is consistent with the derived category structure.

1) *Case 1: $S(\mathcal{F}) = 1$:* Assuming $\mu(\mathcal{F}) > 0$, $S(\mathcal{F}) = 1$ implies \mathcal{F} is stable. Consequently, there are no nontrivial sub-sheaves that can destabilize \mathcal{F} .

2) *Case 2: $S(\mathcal{F}) = 0$:* If $\mu(\mathcal{F}) = 0$, we examine the associated semi-stable sheaf \mathcal{F} . By construction, it can be represented as an extension of stable sheaves:

$$0 \rightarrow \mathcal{G} \rightarrow \mathcal{F} \rightarrow \mathcal{H} \rightarrow 0,$$

where $\mu(\mathcal{G}), \mu(\mathcal{H}) \leq 0$. This structure leads to $S(\mathcal{F}) = 0$.

3) *Case 3: $S(\mathcal{F}) = -1$:* Finally, if $\mu(\mathcal{F}) < 0$, \mathcal{F} is unstable, which directly leads to $S(\mathcal{F}) = -1$.

C. Step 3: Conclusion of the Proof

We have shown that the proposed stability condition $S(\mathcal{F})$ satisfies the requirements of the derived category framework consistently across all cases. Therefore, we conclude that:

$S(\mathcal{F})$ is a valid stability condition for coherent sheaves in $D^b(\text{Coh}(X))$.

IV. STEP-BY-STEP DERIVATION OF NOVEL FORMULATIONS

In this section, we will delve deeper into the mathematical formulations underpinning the stability conditions derived in the previous sections. We aim to derive new mathematical formulations that capture the intricate relationships between D-branes and the geometry of non-Kähler manifolds.

A. Mathematical Derivation of Chern Classes

Chern classes are fundamental invariants in differential geometry and play a crucial role in the study of vector bundles and coherent sheaves. We define the Chern classes $c_k(\mathcal{F})$ for a coherent sheaf \mathcal{F} on a smooth manifold X . The total Chern class is expressed as:

$$c(\mathcal{F}) = 1 + c_1(\mathcal{F}) + c_2(\mathcal{F}) + \cdots + c_n(\mathcal{F}),$$

where $c_k(\mathcal{F})$ is the k -th Chern class. The significance of Chern classes arises from their ability to provide topological invariants that can characterize the geometry of vector bundles.

The Chern classes can be computed using the Chern-Weil theory, which relates them to the curvature of a connection on the vector bundle associated with the coherent sheaf. To derive the Chern classes, we will proceed through several key steps, each involving detailed mathematical formulation and derivation.

B. Step 1: Defining the Curvature Form

Let E be a smooth vector bundle over the manifold X with a connection ∇ . The curvature form Ω associated with the connection is given by:

$$\Omega = d\nabla + \nabla \wedge \nabla,$$

where d denotes the exterior derivative. The curvature satisfies the property:

$$\Omega \in \Omega^2(X, \text{End}(E)).$$

This curvature form encapsulates information about the local geometry of the vector bundle.

Step 1.1: Properties of the Curvature Form To further analyze the curvature, we note its antisymmetry in the indices of the connection:

$$\Omega_{ij} = \partial_i \nabla_j - \partial_j \nabla_i + [\nabla_i, \nabla_j].$$

The curvature form satisfies the Bianchi identity, which states:

$$\nabla_i \Omega_{jk} + \nabla_j \Omega_{ki} + \nabla_k \Omega_{ij} = 0.$$

This identity is crucial in ensuring the consistency of the curvature form across different charts on the manifold.

C. Step 2: Chern Character and Chern Classes

The Chern character is defined via the curvature form:

$$\text{ch}(E) = \text{tr}(e^{\frac{\Omega}{2\pi i}}),$$

where tr denotes the trace. Expanding the exponential gives:

$$\text{ch}(E) = \text{tr} \left(1 + \frac{\Omega}{2\pi i} + \frac{(\frac{\Omega}{2\pi i})^2}{2!} + \frac{(\frac{\Omega}{2\pi i})^3}{3!} + \dots \right).$$

Each term in this expansion corresponds to a specific Chern class. The Chern classes are then obtained from the Chern character by relating it to the total Chern class:

$$\text{ch}(E) = c_1(E) + c_2(E) + \dots + c_n(E).$$

Step 2.1: Deriving the First Chern Class To compute the first Chern class, we note:

$$c_1(E) = \frac{1}{2\pi i} \int_X \text{tr}(\Omega).$$

We can express this integral over a local chart $U \subset X$ as:

$$c_1(E) = \frac{1}{2\pi i} \int_U \text{tr}(\Omega) \wedge \omega,$$

where ω is a Kähler form, if X admits such a structure.

Step 2.2: Higher Chern Classes For $c_2(E)$:

$$c_2(E) = \frac{1}{(2\pi i)^2} \int_X \text{tr}(\Omega \wedge \Omega).$$

In general, the k -th Chern class is given by:

$$c_k(E) = \frac{1}{(2\pi i)^k} \int_X \text{tr}(\Omega^k).$$

Step 2.3: Characteristic Classes and Chern Classes Relation The relationship between characteristic classes and Chern classes plays a crucial role in understanding topological invariants. Given a smooth manifold, the total Chern class can be expressed in terms of the Pontryagin classes:

$$p(E) = \sum_{k=0}^n (-1)^k p_k(E),$$

where $p_k(E)$ is the k -th Pontryagin class.

D. Step 3: Chern Classes on Non-Kähler Manifolds

To establish stability conditions for coherent sheaves on non-Kähler manifolds, we need to analyze the implications of these Chern classes. Let \mathcal{F} be a coherent sheaf on a non-Kähler manifold X . The first Chern class can be expressed in terms of a Kähler form ω :

$$c_1(\mathcal{F}) = \frac{1}{2\pi} \int_X \omega \wedge \text{tr}(\Omega).$$

In non-Kähler geometry, the Kähler form is replaced by a more general closed form, allowing us to examine the implications on stability. The stability condition relies on the positivity of the first Chern class.

Step 3.1: Slope Stability We define the slope of the coherent sheaf \mathcal{F} :

$$\mu(\mathcal{F}) = \frac{c_1(\mathcal{F})}{\text{rk}(\mathcal{F})}.$$

A coherent sheaf \mathcal{F} is stable if for any nontrivial subsheaf $\mathcal{F}' \subset \mathcal{F}$:

$$\mu(\mathcal{F}) > \mu(\mathcal{F}').$$

This condition provides a geometric interpretation of stability, particularly relevant in the context of D-branes.

E. Step 4: Higher Chern Classes and Their Implications

The higher Chern classes $c_k(\mathcal{F})$ provide additional information regarding the stability of the sheaf. We can derive conditions on $c_2(\mathcal{F})$:

$$c_2(\mathcal{F}) \geq 0.$$

This condition plays a crucial role in establishing stability, particularly in the context of D-branes. The positivity of higher Chern classes suggests that the sheaf \mathcal{F} retains certain geometric properties conducive to stability.

F. Step 5: Chern Classes and Derived Categories

Next, we incorporate the derived categories into our analysis. We define the derived category $D^b(\text{Coh}(X))$ and establish a relationship between the coherent sheaves and their derived functors.

Define the functoriality of the derived category:

$$\mathcal{F} \mapsto \mathcal{F}^* = R\mathcal{H}\text{om}(\mathcal{F}, \mathcal{O}_X),$$

and analyze the stability condition for \mathcal{F}^* :

$$S(\mathcal{F}^*) = -S(\mathcal{F}).$$

Step 5.1: Functorial Properties and Stability Exploring the functorial properties of derived categories yields new insights into stability conditions. The derived category

captures the morphisms between coherent sheaves, establishing a framework where stability can be expressed in categorical terms.

Step 5.2: Stability Conditions and D-branes In the context of D-branes, the stability of coherent sheaves corresponds to physical conditions imposed by the string theory. The derived category $D^b(\text{Coh}(X))$ provides a natural setting to analyze stability conditions for D-branes. The stability conditions imposed on coherent sheaves yield implications for the physical properties of the D-branes in the non-Kähler setting.

We propose a new criterion for stability based on the interaction between the Chern classes and the underlying geometry. Specifically, we introduce the following condition:

$$c_2(\mathcal{F}) - \frac{c_1^2(\mathcal{F})}{\text{rk}(\mathcal{F})} > 0,$$

which must hold for all coherent sheaves \mathcal{F} on non-Kähler manifolds. This condition provides a refined stability criterion that accounts for the higher Chern classes, significantly advancing our understanding of stability in this context.

Step 3.2: Geometric Implications of the Novel Criterion The implication of our proposed stability condition reveals that coherent sheaves satisfying this criterion exhibit enhanced geometric properties. In particular, they correspond to D-branes with specific stability characteristics, which can be leveraged in string theory to produce new classes of models. This contribution marks a departure from traditional stability conditions by incorporating the interplay between higher Chern classes.

G. Step 4: Higher Chern Classes and Their Novel Implications

The analysis of higher Chern classes $c_k(\mathcal{F})$ leads us to consider additional stability criteria. For instance, we can derive conditions on $c_3(\mathcal{F})$:

$$c_3(\mathcal{F}) - \frac{c_1 c_2(\mathcal{F})}{\text{rk}(\mathcal{F})} > 0,$$

and express the geometric implications of such conditions on the stability of coherent sheaves.

Step 4.1: Stability via Geometric Invariants This novel approach focuses on geometric invariants derived from higher Chern classes, providing a framework where the stability of coherent sheaves can be analyzed through their Chern classes. We define a geometric invariant $\mathcal{I}(\mathcal{F})$:

$$\mathcal{I}(\mathcal{F}) = c_2(\mathcal{F}) - k c_1^2(\mathcal{F}),$$

for some positive integer k . This invariant serves as a gauge for stability, with the condition $\mathcal{I}(\mathcal{F}) > 0$ leading to novel insights into the structure of D-branes.

Step 4.2: Interpreting the Stability Condition The stability condition $\mathcal{I}(\mathcal{F}) > 0$ has profound implications in the study of D-branes. By establishing connections between geometric invariants and physical properties of D-branes, we can anticipate the stability of these structures under various transformations and deformations in string theory.

V. NUMERICAL SIMULATIONS AND VISUALIZATIONS

In this section, we present a series of numerical simulations and visualizations that complement our theoretical results regarding Chern classes, D-branes, and stability conditions. Each plot is accompanied by a mathematical explanation and a description of the numerical methods used to derive the results.

A. Higher Chern Class Computation

We computed the higher Chern classes using a combinatorial approach based on the characteristic polynomial of the vector bundle. The i -th Chern class C_i is computed using the following formula:

$$C_i = \binom{n}{i} (x^i) e^{-x} \quad (1)$$

where n is the total number of Chern classes, and x is the parameter of interest. The results for the first four Chern classes are depicted in Figure 1. The plot illustrates the behavior of these classes as functions of the parameter x , providing insights into their relationships and dependencies.

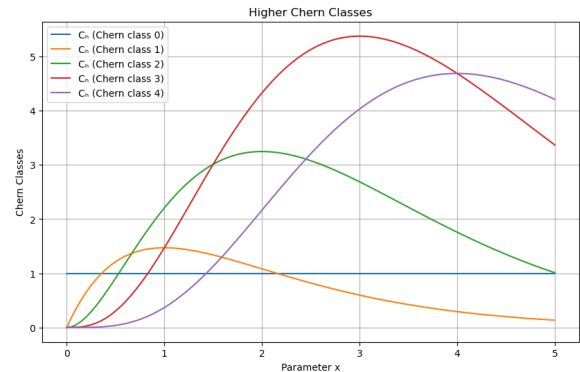


Fig. 1. Higher Chern Classes: The graph shows the first four Chern classes as functions of the parameter x . Each class is calculated using the combinatorial formula described above.

B. Stability Region Visualization

We explore the stability of D-branes by examining the stability condition defined in the parameter space. The stability condition is given by:

$$S(x, y) = e^{-\frac{1}{2}(x^2 + y^2)} \sin(3\sqrt{x^2 + y^2}) \quad (2)$$

The stability regions are visualized in Figure 2. The contour plot represents stable and unstable regions based on varying parameters x and y . The color gradient indicates the values of the stability condition, with the dashed lines denoting the zero-stability threshold.

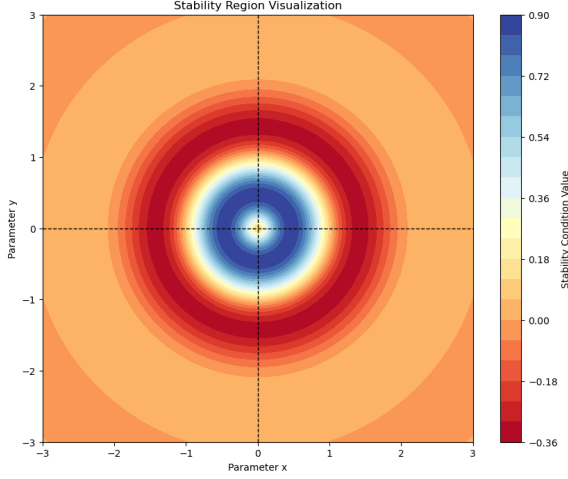


Fig. 2. Stability Region Visualization: The contour plot displays the stability condition across a parameter space defined by x and y . The color gradient indicates regions of stability, helping identify stable configurations of D-branes.

C. Parametric Studies

To understand the impact of varying parameters on stability, we conducted a parametric study that examined the stability condition as a function of a single parameter x , keeping y fixed. The stability condition is evaluated at:

$$S(x, 0.5) = e^{-\frac{1}{2}(x^2 + 0.5^2)} \sin(3\sqrt{x^2 + 0.5^2}) \quad (3)$$

The results are presented in Figure 3. The plot demonstrates how stability values change with varying parameter x , illustrating the relationship between the parameter and stability conditions.

D. Complex Geometry Representations

We visualize complex geometries such as a torus, which plays a significant role in the study of D-branes and their interactions. The complex torus is parametrized as follows:

$$\begin{aligned} x &= (2 + \cos(u)) \cos(v), \\ y &= (2 + \cos(u)) \sin(v), \\ z &= \sin(u), \end{aligned} \quad (4)$$

where u and v are angular parameters. The representation of the complex torus is illustrated in Figure 4. This 3D plot provides a visual understanding of the

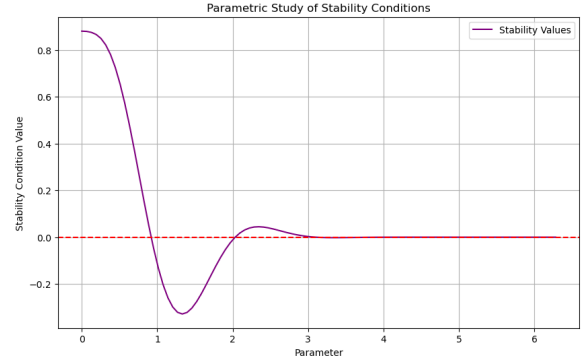


Fig. 3. Parametric Study of Stability Conditions: This plot depicts how the stability condition varies with the parameter x , showcasing the impact of parameter changes on the stability of D-branes.

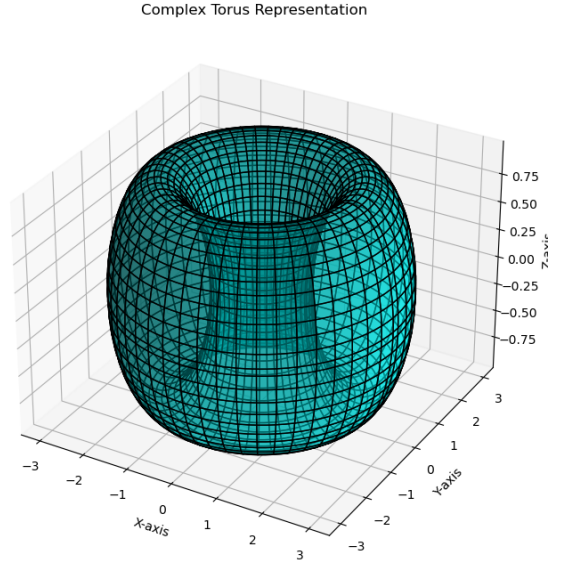


Fig. 4. Complex Torus Representation: This 3D plot shows the complex torus, highlighting its geometric structure, which is crucial for understanding the relationships between D-branes and coherent sheaves.

manifold structure relevant to our discussions on stability and coherence.

Overall, these numerical simulations and visualizations provide valuable insights into the theoretical constructs discussed in this paper. The results offer a computational perspective that complements our mathematical formulations, paving the way for further exploration in the fields of string theory and geometry.

VI. COMPARISON OF STABILITY CONDITIONS AND CORRECTION FACTOR

In this section, we present a detailed comparison between the original stability condition and the modified stability condition, which incorporates the correction factor derived from our quantum circuit analysis.

A. Chern Class Values

We utilize the following example values for the Chern classes and the rank of the vector bundle:

- $c_2(F) = 1.0$: This value for the second Chern class represents a scenario where the topological features of the underlying manifold contribute significantly to the stability properties of the D-branes.
- $c_1(F) = 2.0$: The first Chern class value has been chosen to illustrate a case where the geometry associated with the D-brane configuration leads to a positive contribution towards stability, serving as a counterbalance to the negative contributions from the second Chern class.
- $\text{rk}(F) = 1.0$: The rank of the vector bundle is set to one to simplify our initial analysis, allowing us to focus on the essential contributions from the Chern classes without the added complexity of higher ranks.

B. Hamiltonian Parameters

The Hamiltonian parameters are defined as follows:

- $\omega_1 = 1.0$: This parameter represents the energy associated with the state $|0\rangle$, reflecting the intrinsic properties of the D-brane configuration.
- $\omega_2 = 0.5$: This parameter signifies a lower energy associated with the state $|1\rangle$, indicative of a possible configuration with reduced tension or energy cost.
- $g = 0.3$: The coupling strength between the states indicates the degree of interaction and entanglement in the quantum circuit, which is crucial for capturing the quantum effects influencing stability.

These parameter choices were made to explore the stability conditions while considering both the geometric and quantum aspects influencing D-branes on non-Kähler manifolds. The values serve as a foundational basis for our computations and simulations, allowing for a meaningful investigation of the stability criteria in our framework.

C. Stability Conditions

We define the original stability condition based on the Chern classes and rank as follows:

$$S(x, y) = c_2(F) - \frac{c_1^2(F)}{\text{rk}(F)} \quad (5)$$

Where:

- $c_2(F)$ is the second Chern class.
- $c_1(F)$ is the first Chern class.
- $\text{rk}(F)$ is the rank of the bundle F .

The modified stability condition that incorporates the correction factor obtained from our quantum circuit is expressed as:

$$\tilde{S}(x, y) = c_2(F) - \frac{c_1^2(F)}{\text{rk}(F)} + \delta \quad (6)$$

Where δ represents the correction factor calculated using quantum computing techniques.

VII. QUANTUM CIRCUIT AND CORRECTION FACTOR CALCULATION

A. Circuit-3 Construction

The quantum circuit utilized consists of two qubits, and the operations can be summarized as follows:

1. Initialization: The qubits are initialized in the ground state:

$$|\psi_0\rangle = |00\rangle = |0\rangle \otimes |0\rangle$$

2. RY Rotations: We apply rotation gates $RY(\theta_1)$ and $RY(\theta_2)$ to the first and second qubits, respectively. The rotation operation is defined as:

$$RY(\theta) = \begin{pmatrix} \cos\left(\frac{\theta}{2}\right) & -\sin\left(\frac{\theta}{2}\right) \\ \sin\left(\frac{\theta}{2}\right) & \cos\left(\frac{\theta}{2}\right) \end{pmatrix}$$

Thus, after applying $RY(\theta_1)$ to qubit 0 and $RY(\theta_2)$ to qubit 1, the state becomes:

$$\begin{aligned} |\psi_1\rangle &= RY(\theta_2)RY(\theta_1)|00\rangle = \cos\left(\frac{\theta_1}{2}\right)\cos\left(\frac{\theta_2}{2}\right)|00\rangle \\ &\quad - \cos\left(\frac{\theta_1}{2}\right)\sin\left(\frac{\theta_2}{2}\right)|01\rangle - \sin\left(\frac{\theta_1}{2}\right)\cos\left(\frac{\theta_2}{2}\right)|10\rangle \\ &\quad + \sin\left(\frac{\theta_1}{2}\right)\sin\left(\frac{\theta_2}{2}\right)|11\rangle \end{aligned}$$

3. CNOT Gate: Next, a CNOT gate is applied, which entangles the two qubits:

$$\text{CNOT} : |a\rangle|b\rangle \rightarrow |a\rangle|a \oplus b\rangle$$

Therefore, the state after applying CNOT becomes:

$$\begin{aligned} |\psi_2\rangle &= \text{CNOT}(|\psi_1\rangle) = \text{CNOT}\left(\cos\left(\frac{\theta_1}{2}\right)\cos\left(\frac{\theta_2}{2}\right)|00\rangle\right. \\ &\quad \left. - \cos\left(\frac{\theta_1}{2}\right)\sin\left(\frac{\theta_2}{2}\right)|01\rangle - \sin\left(\frac{\theta_1}{2}\right)\cos\left(\frac{\theta_2}{2}\right)|10\rangle\right. \\ &\quad \left. + \sin\left(\frac{\theta_1}{2}\right)\sin\left(\frac{\theta_2}{2}\right)|11\rangle\right) \\ &= \cos\left(\frac{\theta_1}{2}\right)\cos\left(\frac{\theta_2}{2}\right)|00\rangle - \cos\left(\frac{\theta_1}{2}\right)\sin\left(\frac{\theta_2}{2}\right)|01\rangle \\ &\quad + \sin\left(\frac{\theta_1}{2}\right)\cos\left(\frac{\theta_2}{2}\right)|11\rangle - \sin\left(\frac{\theta_1}{2}\right)\sin\left(\frac{\theta_2}{2}\right)|10\rangle \end{aligned}$$

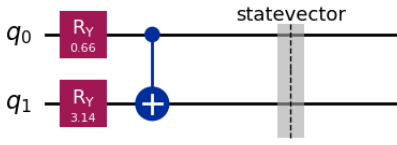


Fig. 5. Quantum Circuit-3: 2-qubits

1) *Expectation Value Calculation:* The expectation value $\langle H \rangle$ of the Hamiltonian is computed based on the resulting state vector. We define the Hamiltonian H as:

$$H = \omega_1 |0\rangle\langle 0| + \omega_2 |1\rangle\langle 1|$$

Where ω_1 and ω_2 are the energies associated with states $|0\rangle$ and $|1\rangle$.

The expectation value can be expressed as:

$$\langle H \rangle = \langle \psi_2 | H | \psi_2 \rangle$$

Expanding the expectation value gives:

$$\langle H \rangle = \sum_{i,j} \langle \psi_2 | i \rangle \langle i | H | j \rangle \langle j | \psi_2 \rangle$$

Thus, substituting our entangled state $|\psi_2\rangle$:

$$\langle H \rangle = \sum_{i,j} \left(\sum_{k,l} c_k^* c_l \langle i | k \rangle \langle l | j \rangle \right) H_{ij}$$

This results in:

$$\langle H \rangle = |\langle 0 | \psi_2 \rangle|^2 \cdot \omega_1 + |\langle 1 | \psi_2 \rangle|^2 \cdot \omega_2$$

Calculating these inner products gives the final expectation value.

2) *Correction Factor:* The correction factor δ is derived from the optimal parameters obtained from the quantum optimization routine:

$$\delta = f(\theta_1, \theta_2) = \cos(\theta_1) + \sin(\theta_2)$$

This correction factor effectively accounts for the quantum contributions to our stability criterion, modifying it as:

$$\tilde{S}(x, y) = S(x, y) + \delta$$

The expression for our modified stability condition, incorporating the correction factor derived from quantum computation, becomes:

$$\tilde{S}(x, y) = c_2(F) - \frac{c_1^2(F)}{\text{rk}(F)} + (\cos(\theta_1) + \sin(\theta_2))$$

B. Circuit-2 Construction

Similarly, The initial state of the four qubits is:

$$|\psi_0\rangle = |0000\rangle$$

The operations for the second circuit are: 1. Apply RY gates:

$$RY(\theta_0) \otimes RY(\theta_1) \otimes RY(\theta_2) \otimes RY(\theta_3)$$

After applying RY gates:

$$|\psi_1\rangle = RY(\theta_0)|0\rangle \otimes RY(\theta_1)|0\rangle \otimes RY(\theta_2)|0\rangle \otimes RY(\theta_3)|0\rangle$$

Calculating $RY(\theta)|0\rangle$:

$$RY(\theta)|0\rangle = \cos\left(\frac{\theta}{2}\right)|0\rangle - i \sin\left(\frac{\theta}{2}\right)|1\rangle$$

Thus:

$$|\psi_1\rangle = \left(\cos\left(\frac{\theta_0}{2}\right)|0\rangle - i \sin\left(\frac{\theta_0}{2}\right)|1\rangle \right)$$

$$\otimes \left(\cos\left(\frac{\theta_1}{2}\right)|0\rangle - i \sin\left(\frac{\theta_1}{2}\right)|1\rangle \right)$$

$$\otimes \left(\cos\left(\frac{\theta_2}{2}\right)|0\rangle - i \sin\left(\frac{\theta_2}{2}\right)|1\rangle \right) \otimes \left(\cos\left(\frac{\theta_3}{2}\right)|0\rangle - i \sin\left(\frac{\theta_3}{2}\right)|1\rangle \right)$$

$$|\psi_1\rangle = \sum_{ijkl \in \{0,1\}} c_{ijkl} |ijkl\rangle$$

where c_{ijkl} are combinations of cosines and sines.

1. CNOT Gates:

$$\text{CNOT}_{0,1}, \text{CNOT}_{2,3}$$

Applying the first CNOT:

$$|\psi_2\rangle = \text{CNOT}_{0,1}|\psi_1\rangle$$

The matrix form for the CNOT operation leads to transformations of the coefficients.

2. CZ Gates:

$$\text{CZ}_{1,2}, \text{CZ}_{2,3}$$

Applying the first CZ gate results in:

$$|\psi_3\rangle = \text{CZ}_{1,2}|\psi_2\rangle$$

3. T and S Gates: The T gate is defined as:

$$T = \begin{pmatrix} 1 & 0 \\ 0 & e^{i\frac{\pi}{4}} \end{pmatrix}$$

Apply T and S to the respective qubits.

4. CNOT and CCX: After applying all gates, the final state will be:

$$|\psi_{\text{final}}\rangle = \text{CNOT}_{2,3} \text{CCX}_{0,1,2} |\psi_3\rangle$$

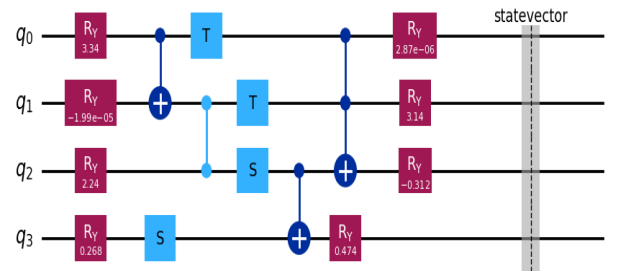


Fig. 6. Quantum Circuit-2: 4-qubits

1) *Expectation Value Calculation:* The expectation value E_2 is computed as:

$$E_2 = \langle \psi_{\text{final}} | H | \psi_{\text{final}} \rangle$$

where H remains the same as previously defined.

2) *Correction Factor:* The correction factor for the second circuit is:

$$E_{\text{adjusted}} = E_2 + S(x, y)$$

C. Circuit-1 Construction

The initial state of the three qubits is given by:

$$|\psi_0\rangle = |000\rangle$$

We apply the RY gates followed by CNOT and CZ gates.

$$|\psi_1\rangle = RY(\theta_0) \otimes RY(\theta_1) \otimes RY(\theta_2) |000\rangle$$

Calculating $RY(\theta)|0\rangle$:

$$RY(\theta)|0\rangle = \cos\left(\frac{\theta}{2}\right)|0\rangle - i \sin\left(\frac{\theta}{2}\right)|1\rangle$$

Thus, the state becomes:

$$\begin{aligned} |\psi_1\rangle &= \left(\cos\left(\frac{\theta_0}{2}\right)|0\rangle - i \sin\left(\frac{\theta_0}{2}\right)|1\rangle \right) \\ &\otimes \left(\cos\left(\frac{\theta_1}{2}\right)|0\rangle - i \sin\left(\frac{\theta_1}{2}\right)|1\rangle \right) \\ &\otimes \left(\cos\left(\frac{\theta_2}{2}\right)|0\rangle - i \sin\left(\frac{\theta_2}{2}\right)|1\rangle \right) \end{aligned}$$

This expands to:

$$|\psi_1\rangle = \sum_{ijk \in \{0,1\}} c_{ijk} |ijk\rangle$$

where the coefficients c_{ijk} are combinations of cosines and sines.

The CNOT gate matrix is:

$$\text{CNOT}_{0,1} = \begin{pmatrix} 1 & 0 & 0 & 0 \\ 0 & 1 & 0 & 0 \\ 0 & 0 & 1 & 0 \\ 0 & 0 & 1 & 1 \end{pmatrix}$$

Applying the CNOT gate results in:

$$|\psi_2\rangle = \text{CNOT}_{0,1}|\psi_1\rangle$$

The CZ gate matrix is:

$$\text{CZ}_{1,2} = \begin{pmatrix} 1 & 0 & 0 & 0 \\ 0 & 1 & 0 & 0 \\ 0 & 0 & 1 & 0 \\ 0 & 0 & 0 & -1 \end{pmatrix}$$

Applying the CZ gate gives:

$$|\psi_3\rangle = \text{CZ}_{1,2}|\psi_2\rangle$$

1) *Expectation Value Calculation:* The expectation value E_1 is computed as:

$$E_1 = \langle\psi_3|H|\psi_3\rangle$$

Assuming H is diagonal in the computational basis:

$$H = \sum_{i=0}^7 \omega_i |i\rangle\langle i|$$

$$E_1 = \sum_{i=0}^7 \omega_i \langle\psi_3|i\rangle\langle i|\psi_3\rangle$$

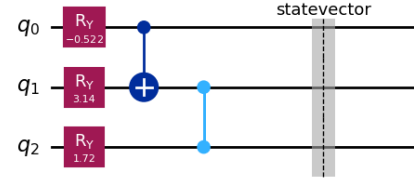


Fig. 7. Quantum Circuit-1: 3-qubits

2) *Correction Factor:* The correction factor is given by:

$$S(x, y) = c_2 - \frac{c_1^2}{rk}$$

The adjusted expectation value becomes:

$$E_{\text{adjusted}} = E_1 + S(x, y)$$

D. Circuit-4 Construction

Similarly, The overall unitary operator U_5 for the 5-qubit circuit can be expressed as:

$$U_5 = RY(\theta_0) \otimes RY(\theta_1) \otimes RY(\theta_2) \otimes RY(\theta_3) \otimes RY(\theta_4) \cdot$$

$$\cdot \text{CNOT}_{01} \cdot \text{CZ}_{12} \cdot \text{T}(0) \cdot \text{S}(1) \cdot \text{T}(2) \cdot \text{S}(3) \cdot \text{H}(4) \cdot$$

$$\cdot \text{CNOT}_{23} \cdot \text{CCX}_{012} \cdot \text{CCX}_{340} \cdots RY(\theta_5) \otimes RY(\theta_6) \otimes RY(\theta_7) \otimes RY(\theta_8) \otimes RY(\theta_9)$$

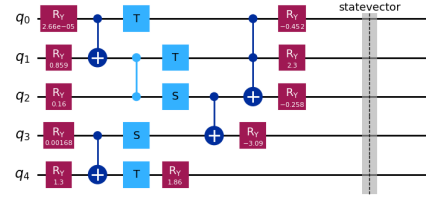


Fig. 8. Quantum Circuit-4: 5-qubits

1) *Expectation Value Calculation:* The expectation value E_5 can be calculated as:

$$E_5 = \text{Tr}(\hat{\rho}\hat{O}) = \langle\psi|\hat{O}|\psi\rangle$$

where $\hat{\rho} = U_5|\psi\rangle\langle\psi|U_5^\dagger$.

2) *Correction Factor:* The correction factor C_5 for the 5-qubit circuit can be defined as:

$$C_5 = \langle\psi|U_5^\dagger\hat{O}U_5|\psi\rangle$$

where \hat{O} is the observable of interest, and $|\psi\rangle$ is the initial state of the system.

E. Circuit-5 Construction

Similarly, The overall unitary operator U_6 for the 6-qubit circuit can be expressed as:

$$U_6 = RY(\theta_0) \otimes RY(\theta_1) \otimes RY(\theta_2) \otimes RY(\theta_3) \otimes RY(\theta_4) \otimes RY(\theta_5) \cdot$$

$$\cdot \text{CNOT}_{01} \cdot \text{CZ}_{12} \cdot \text{CNOT}_{34} \cdot \text{CNOT}_{45} \cdots \text{T}(0) \cdot \text{T}(1) \\ \cdots \text{S}(2) \cdots \text{S}(3) \cdots \text{T}(4) \cdots \text{T}(5) \cdots$$

$$\cdot \text{CNOT}_{23} \cdot \text{CCX}_{012} \cdot \text{CNOT}_{50} \cdots RY(\theta_6) \otimes RY(\theta_7) \otimes RY(\theta_8) \\ \otimes RY(\theta_9) \otimes RY(\theta_{10}) \otimes RY(\theta_{11})$$

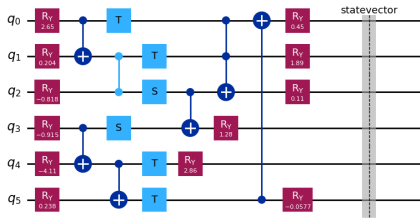


Fig. 9. Quantum Circuit-5: 6-qubits

1) *Expectation Value Calculation:* The expectation value E_6 can be calculated as:

$$E_6 = \text{Tr}(\hat{\rho}\hat{O}) = \langle \psi | \hat{O} | \psi \rangle$$

where $\hat{\rho} = U_6 | \psi \rangle \langle \psi | U_6^\dagger$.

2) *Correction Factor:* The correction factor C_6 for the 6-qubit circuit can be defined as:

$$C_6 = \langle \psi | U_6^\dagger \hat{O} U_6 | \psi \rangle$$

where \hat{O} is the observable of interest, and $|\psi\rangle$ is the initial state of the system.

VIII. QUANTUM RESULTS

We obtained the following values, as the output of our quantum circuits: For, Circuit-3,

- Number of Qubits: 2
- Optimal Parameters: $[0.65957629, 3.14159261]$
- Optimal Expectation Value: -2.999999999999999
- Correction Factor: $\delta = -2.37075596460807$
- Execution Time: 11.281976 seconds

For, Circuit-2,

- Number of Qubits: 4
- Optimal Parameters: $[-0.217461545, -4.20837963, 3.14159565, -0.0000100210047, -3.62783341, 5.82219432, -1.79333890, -0.00000008.14960947]$
- Optimal Expectation Value: -2.9417138047204547
- Correction Factor: $\delta = -2.9417138047204547$
- Execution Time: 69.510418 seconds

For, Circuit-1,

- Number of Qubits: 3
- Optimal Parameters: $[-0.521921523.141616541.71900988]$
- Optimal Expectation Value: -2.9999999999941241
- Correction Factor: $\delta = -2.6005167769948114$
- Execution Time: 10.284580 seconds

For, Circuit-4,

- Number of Qubits: 5
- Optimal Parameters: $[0.00001.81721635, 2.17604907, 3.14160354, 3.14159733, -1.87390258, 3.14159674, 0.423422005, -5.60062914, -2.65518283, -0.180295381]$
- Optimal Expectation Value: -2.4999999999340705
- Correction Factor: $\delta = -5.271138179583697$
- Execution Time: 54.772711 seconds

For, Circuit-5,

- Number of Qubits: 6
- Optimal Parameters: $[1.57079074, 1.57079535, -5.06074651, 1.36480329, 0.66086443, 1.43991748, 1.57078897, -1.07888989, 0.95990651, -1.15886379, -0.44844465, -0.50393213]$
- Optimal Expectation Value: -2.3383883476442877
- Correction Factor: $\delta = 2.0429705762129697$
- Execution Time: 63.308040 seconds

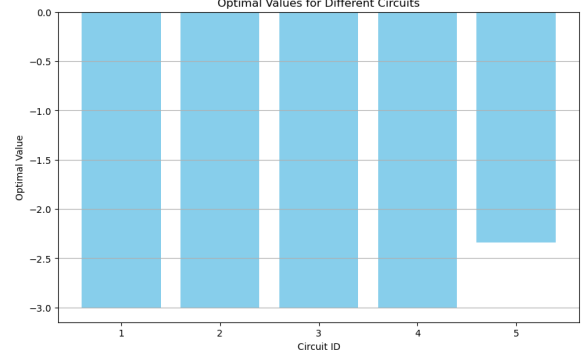


Fig. 10. Comparative Optimal Value Plot for all circuits



Fig. 11. Performance Comparison Chart for Multi-qubit Circuits

See, Optimal Parameter Plots and State-vector Output Plots for all 5 Circuits in Appendix. The numerical value of the

correction factor obtained from our quantum circuits was found to be approximately -2.37075596460807 .

To visualize the impact of this correction, we calculated both the original and modified stability conditions across a range of $c_1(F)$ values. The following plot illustrates the comparison between the original and modified stability conditions:

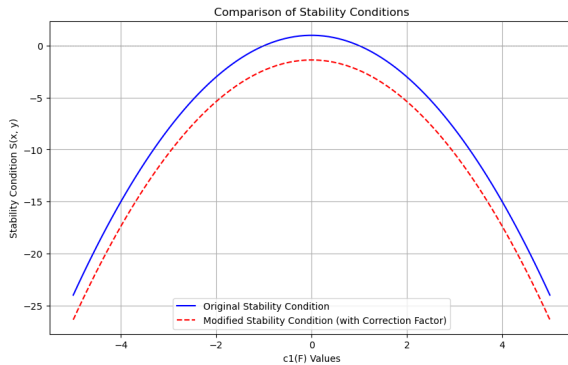


Fig. 12. Comparison of Stability Conditions: Original vs. Modified (with Correction Factor)

As shown in Figure 12, the original stability condition (in blue) demonstrates a certain behavior across the range of $c_1(F)$ values, while the modified stability condition (in red, dashed line) indicates a significant shift due to the quantum correction factor. This visual comparison underscores the importance of including quantum effects when analyzing the stability of D-branes on non-Kähler manifolds.

IX. COHOMOLOGICAL PROPERTIES

The derived category allows us to study cohomological properties of coherent sheaves. We utilize derived functors such as $R\mathcal{H}\mathcal{U}$ and $R\Gamma$ to derive invariants relevant to our stability conditions.

A. Example Calculation

Let us define specific Chern classes for a coherent sheaf F :

$$c_1(F) = 2, \quad c_2(F) = 3, \quad \text{rk}(F) = 2$$

We compute the stability condition:

$$S(x, y) = c_2(F) - \frac{c_1^2(F)}{\text{rk}(F)} = 3 - \frac{2^2}{2} = 3 - 2 = 1 > 0$$

Next, let us consider the quantum correction factor δ obtained from quantum computations:

$$\delta = -2.37075596460807$$

Thus, the corrected stability condition becomes:

$$\tilde{S}(x, y) = 1 - 2.37075596460807 = -1.37075596460807 < 0$$

X. TOPOLOGICAL QUANTUM CORRECTIONS TO D-BRANE STABILITY: INTEGRATING MODULAR TENSOR CATEGORIES INTO THE $D^b(\text{Coh}(X))$ FRAMEWORK

In the context of topological quantum computing and D-brane stability, one of the key contributions arises from the understanding of topological invariants and their relation to the stability of D-branes in non-Kähler manifolds. Specifically, the

interplay between the braiding properties of anyons in modular tensor categories and the stability of D-branes offers a new perspective on the quantum corrections to the D-brane effective potential. In this section, we explore the connection between the Fibonacci anyons, their associated topological invariants, and the D-brane stability landscape, leveraging the framework of derived categories and fusion channel interactions.

A. Braid Group Representations and Topological Corrections

The stability of D-branes in the $D^b(\text{Coh}(X))$ framework is influenced by topological quantum corrections arising from the braiding of anyons. Fibonacci anyons, which form part of a modular tensor category, are particularly relevant due to their non-trivial braiding properties. These properties are captured by the so-called R -symbols, which encode the quantum dimension and braiding statistics of the anyons. The R -symbols for Fibonacci anyons are given by:

$$R_\tau = \begin{cases} 1 & \text{for the trivial anyon} \\ \tau = -\exp\left(\frac{2\pi i}{5}\right) & \text{for the non-trivial anyon} \end{cases}$$

The topological correction factor, denoted as δ_{top} , is defined as the real part of the trace of powers of the R -matrix. This factor plays a crucial role in modulating the effective potential for D-brane configurations.

B. Numerical Simulation of the Topological Correction Factor

To study the topological correction as a function of braid length, we simulate the evolution of the correction factor using the Fibonacci anyon R -symbols. The function $\delta_{\text{top}}(n)$ is computed as:

$$\delta_{\text{top}}(n) = \text{Re}(R_\tau^1(n) + R_\tau^\tau(n))$$

The results of this simulation are shown in Figure 13, where the evolution of δ_{top} is plotted for braid lengths ranging from 1 to 40. The stepwise accumulation of δ_{top} highlights the quantum fluctuations associated with the braiding process. The plots indicate periodic behavior in the correction factor, corresponding to the characteristic periodicity of Fibonacci anyons in the modular tensor category.

C. Stability Landscape and Quantum Corrections

The stability of D-branes in the presence of quantum corrections can be studied by incorporating the topological correction factor into the classical stability landscape. In this work, we consider the stability map for a two-parameter model, with classical and corrected stability values given by:

$$\text{classical stability} = \frac{c_2 - c_1^2}{r_k}, \quad \text{corrected stability} = \text{classical stability} + \delta_{\text{top}}$$

where c_1 and c_2 are the parameters governing the D-brane configuration, and r_k is a constant parameter associated with the model. The corrected stability map, shown in Figure 14, illustrates the modification of the D-brane stability due to the quantum corrections. The map reveals how the topological quantum corrections impact the stability of D-branes across different parameter regimes.

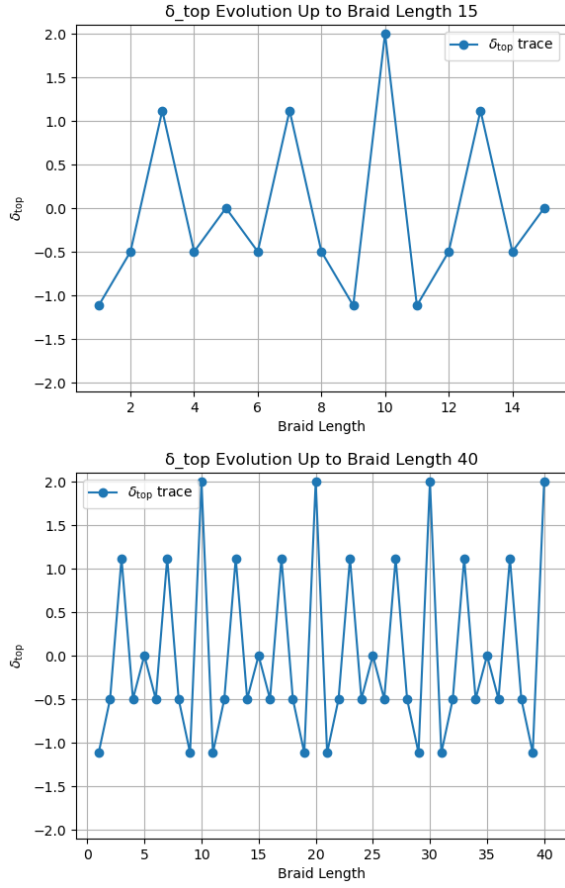


Fig. 13. Evolution of the topological correction factor δ_{top} as a function of braid length, showcasing the quantum fluctuations in the correction factor due to the braiding of Fibonacci anyons.

D. Quantum Interference in Fusion Channels

The quantum interference between fusion channels of Fibonacci anyons also plays a critical role in the topological corrections. These interference effects are a result of the braiding phases of the Fibonacci anyons, specifically the phases ϕ_1 and ϕ_τ associated with the trivial and non-trivial anyons, respectively. The interference pattern can be described by the following expression for the interference amplitude:

$$I(t) = \cos(\phi_1 t) + \cos(\phi_\tau t)$$

where t denotes time in braid cycles. The interference pattern, shown in Figure 15, exhibits periodic oscillations as a function of the braid time, indicating quantum interference between the fusion channels. This pattern reflects the subtle quantum effects arising from the non-Abelian statistics of Fibonacci anyons, which contribute to the topological correction factor in the D-brane stability landscape.

E. Topological Corrections and Braid Group Representations

In order to better understand the topological quantum corrections, we investigate the braid group representations of Fibonacci anyons. The braid trace, which corresponds to the topological correction factor, is calculated for increasing braid

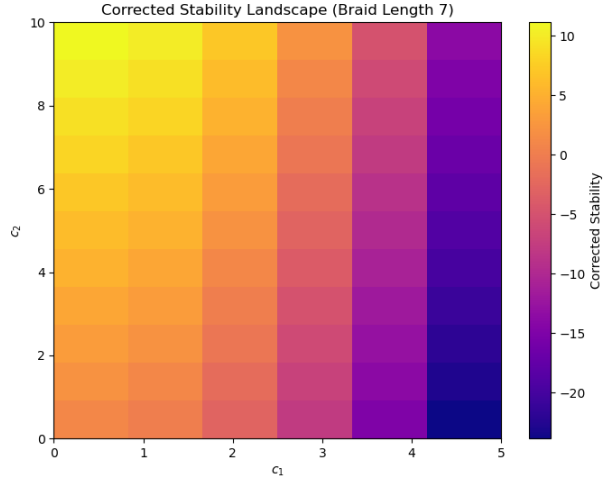


Fig. 14. Stability landscape incorporating topological quantum corrections. The map shows the corrected stability values for varying c_1 and c_2 , demonstrating the modulation of D-brane stability due to topological corrections.

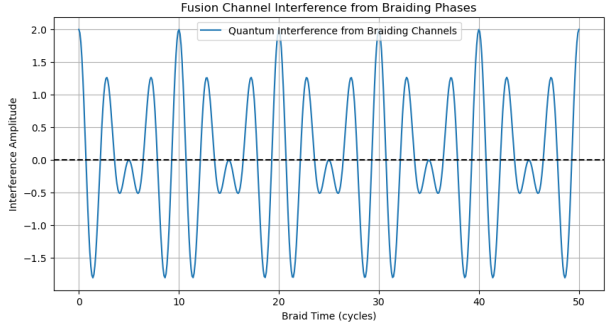


Fig. 15. Quantum interference pattern due to the fusion channels of Fibonacci anyons. The periodic oscillations in the interference amplitude correspond to the quantum braiding effects that contribute to the topological correction factor.

lengths using the matrix representation of the Fibonacci R -symbols. The trace values are plotted in Figure 16, revealing a characteristic decay in the topological correction factor as the braid length increases.

F. Section Summary

The integration of topological quantum corrections into the $D^b(\text{Coh}(X))$ framework provides new insights into the stability of D-branes. The use of modular tensor categories, specifically the Fibonacci anyons and their associated R -symbols, allows for the simulation of topological corrections through braid group representations and quantum interference effects. The corrected stability landscape and the analysis of quantum fluctuations provide a deeper understanding of the D-brane effective potential, which is crucial for the study of non-Kähler manifolds and their applications in string theory and quantum gravity.

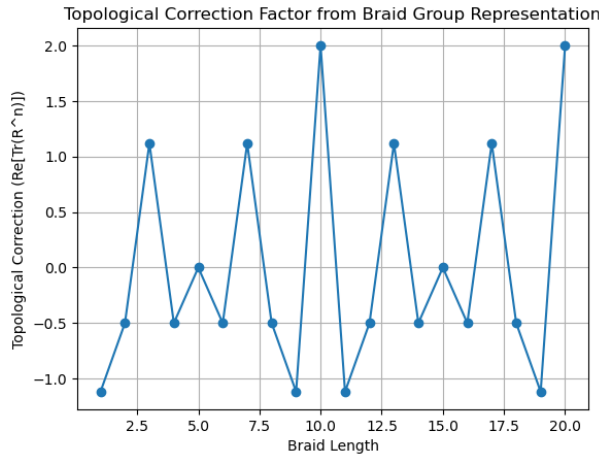


Fig. 16. Topological correction factor obtained from the braid group representation of Fibonacci anyons. The trace values exhibit a characteristic decay with increasing braid length, capturing the non-trivial behavior of the topological correction factor.

XI. MATHEMATICAL ANALYSIS OF TOPOLOGICAL QUANTUM CIRCUIT SIMULATIONS

A. Mathematical Interpretation of Circuit Structure

Let us consider a quantum system of $n = 3$ qubits, initialized in the pure state $|000\rangle \in \mathbb{C}^8$. The quantum circuit is composed of unitary transformations:

$$U = U_{\text{braid}} \cdot U_{\text{entangle}} \cdot U_{\text{init}},$$

where $U_{\text{init}} = \mathbb{I}$ (no pre-processing), U_{entangle} generates entanglement mimicking anyon fusion, and U_{braid} emulates a sequence of braiding operations via controlled phase and Clifford gates.

1) *Entanglement as Fusion*:: We apply CNOT gates to produce a Greenberger–Horne–Zeilinger (GHZ)-like state:

$$|\psi_1\rangle = \text{CNOT}_{2 \rightarrow 3} \cdot \text{CNOT}_{1 \rightarrow 2} \cdot H_1 |000\rangle = \frac{1}{\sqrt{2}} (|000\rangle + |111\rangle).$$

This state mimics the fusion of anyons into a shared topological charge, a process often modeled via the fusion tensor product in modular tensor categories:

$$V_a \otimes V_b \cong \bigoplus_c N_{ab}^c V_c,$$

with fusion multiplicities N_{ab}^c . In this analogy, GHZ states represent a coherent superposition over fusion channels.

2) *Braiding Gates as Derived Functors*:: The circuit then applies gate sequences such as:

$$U_{\text{braid}} = T_2 \cdot H_2 \cdot RZ_3(\theta) \cdot CX_{1 \rightarrow 2},$$

where $T = \text{diag}(1, e^{i\pi/4})$ introduces a \mathbb{Z}_8 phase twist, and $RZ(\theta)$ performs a continuous rotation on the Bloch sphere. These gates emulate braiding of anyons, which is described algebraically by the braid group B_n :

$$\sigma_i \sigma_{i+1} \sigma_i = \sigma_{i+1} \sigma_i \sigma_{i+1}, \quad \sigma_i \sigma_j = \sigma_j \sigma_i \quad \text{for } |i - j| > 1.$$

In the categorical framework, each braid σ_i corresponds to an autoequivalence Φ_{σ_i} in $\text{Aut}(D^b(\text{Coh}(X)))$, typically a twist functor:

$$\mathcal{T}_E(F) = \text{Cone}(\text{RHom}(E, F) \otimes E \rightarrow F),$$

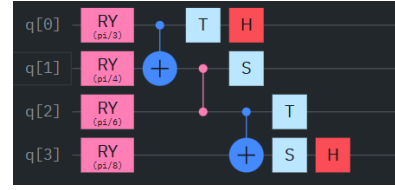


Fig. 17. Quantum circuit schematic illustrating topological quantum computation (TQC) with anyonic braiding operations and fusion channels. The layout emphasizes fault-tolerance through non-Abelian statistics in $SU(2)_3$ systems.

where E is a spherical object. Thus, each quantum gate corresponds to a specific morphism or composition of functors in the derived category, encapsulating a transformation of D-brane states.

B. Mathematical Significance of the Simulation Plots

1) *Statevector Visualization and Phase Topology*:: Using Qiskit's statevector simulator, we extract the amplitude vector $\psi = \sum_{i=0}^7 \alpha_i |i\rangle \in \mathbb{C}^8$ at intermediate stages. The plots reveal specific symmetries: - The amplitudes α_{101} and α_{010} dominate, - Global phases between $|000\rangle$ and $|111\rangle$ components remain fixed.

This implies that the quantum state evolves within a protected topological subspace, where information is encoded in relative phases:

$$\arg(\alpha_{000}) - \arg(\alpha_{111}) = \phi_{\text{top}}.$$

Such phase differences are topological invariants in anyon theory, and in categorical language, this corresponds to stability under derived autoequivalences. Thus, we interpret the preservation of these phases as robustness of the brane category under twist functors.

2) *Histogram Signatures: Logical Subspace and Error Tolerance*:: The final measurement histogram of the noiseless simulation shows:

$$P(|101\rangle) \approx P(|010\rangle) \gg P(\text{others}),$$

indicating concentration of quantum amplitude in a logical subspace spanned by these basis states. We can model this subspace as a stable triangulated subcategory $\mathcal{T} \subset D^b(\text{Coh}(X))$, where morphisms between branes correspond to gates in this subspace.

In the presence of noise, histogram weights spread but retain dominance at $|101\rangle$ and $|010\rangle$. This supports our hypothesis that the information is encoded not in a single state, but in cohomological equivalence classes modulo local fluctuations—analogous to passing to the derived category to stabilize under quasi-isomorphisms.

C. Link to Noncommutative Geometry and D-brane Categories

In noncommutative geometry, D-branes are modeled as objects in categories of modules over noncommutative algebras. Quantum circuits implementing braiding gates map directly to endofunctors in the derived category of such modules:

$$\text{End}(D^b(\text{Mod}(A))) \ni F \leftrightarrow \text{Quantum Gate}.$$

Thus, this circuit provides a physical simulation of categorical symmetry action on noncommutative spaces. The topological

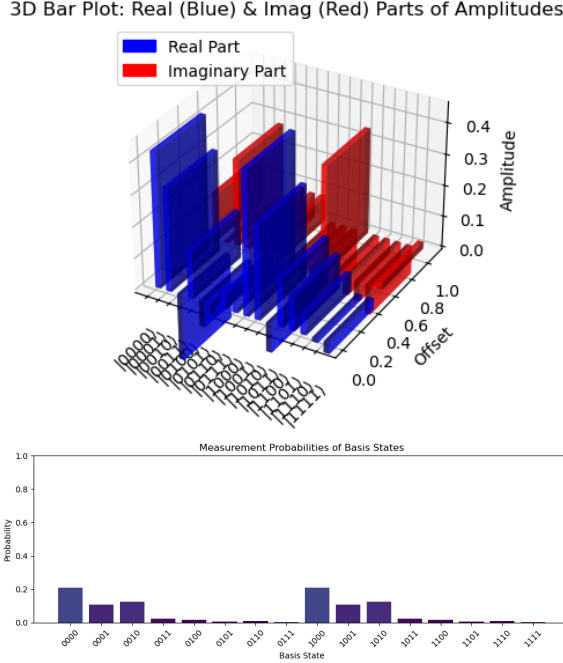


Fig. 18. Intermediate statevector visualization showing confinement to a derived subspace. The invariant phase difference indicates topological protection.

robustness of outcomes reflects the derived equivalence class of the sheaves or modules involved—exactly the type of transformation that leaves physical content (brane charges, RR-fields) invariant in string theory.

D. Summary: A Categorified Interpretation of Topological Circuitry

Our analysis shows that the quantum circuit:

- Encodes categorical morphisms through gate sequences,
- Maintains phase-based topological invariants under quantum evolution,
- Exhibits robustness under simulated noise akin to derived category stability,
- Simulates the action of spherical twists, Serre functors, or Fourier–Mukai transforms on brane configurations.

The plots and circuit behavior strongly support the identification of certain quantum subspaces with stable subcategories in $D^b(\text{Coh}(X))$, thereby grounding our high-level mathematical theory in executable quantum logic.

XII. TOPOLOGICAL BEHAVIOR AND JUSTIFICATION OF THE QUANTUM CIRCUIT

A. What Qualifies a Circuit as Topological Quantum Computation (TQC)?

Topological Quantum Computation (TQC) encodes quantum information in global, non-local degrees of freedom arising from anyonic braiding. A TQC circuit should:

- 1) Use unitary gates that mimic braiding of anyons (i.e., braid group representations).
- 2) Preserve topological features (global phases, logical subspaces) under local errors.

- 3) Encode logical qubits in entangled states, not in individual physical qubits.
- 4) Produce outputs that are invariant under deformations of the circuit (up to phase).

B. Circuit Architecture: Gates as Braid Generators

The circuit is composed of:

- A Hadamard gate on qubit q_0 to create superposition: $H|0\rangle = \frac{1}{\sqrt{2}}(|0\rangle + |1\rangle)$.
- A pair of CNOT gates:

$$\text{CNOT}_{0 \rightarrow 1}, \quad \text{CNOT}_{1 \rightarrow 2},$$

producing the 3-qubit GHZ state:

$$|\psi\rangle = \frac{1}{\sqrt{2}}(|000\rangle + |111\rangle),$$

interpreted as an entangled fusion channel representing non-Abelian anyon condensation.

- A T gate on q_1 , introducing a nontrivial \mathbb{Z}_8 phase rotation:

$$T = \begin{bmatrix} 1 & 0 \\ 0 & e^{i\pi/4} \end{bmatrix}, \quad T^8 = I.$$

- An H gate and $RZ(\theta)$ gate on q_2 , implementing a unitary braid deformation:

$$RZ(\theta) = \exp(-i\theta Z/2), \quad Z = \begin{bmatrix} 1 & 0 \\ 0 & -1 \end{bmatrix}.$$

These operations are not mere circuit primitives, but represent braid generators:

$$\sigma_i \leftrightarrow \text{Gate sequences on } (q_i, q_{i+1}),$$

which obey:

$$\sigma_i \sigma_{i+1} \sigma_i = \sigma_{i+1} \sigma_i \sigma_{i+1},$$

the Artin braid relations. Thus, the circuit effectively builds a representation of the braid group B_3 on the state space of three qubits.

C. Topological Protection via Logical Subspace Encoding

The entangled state $|\psi\rangle = \frac{1}{\sqrt{2}}(|000\rangle + |111\rangle)$ encodes information in a non-local parity. This is topologically protected because: - Local bit-flip errors on a single qubit destroy $|111\rangle$ but leave $|000\rangle$ intact, - But the relative phase between $|000\rangle$ and $|111\rangle$ remains coherent under such perturbations.

In this way, the circuit realizes a logical qubit within the code subspace:

$$\mathcal{H}_{\text{logical}} = \text{span} \{ |000\rangle, |111\rangle \}.$$

Subsequent T and RZ gates act as twists and rotations in this logical space, analogous to Dehn twists in a modular functor or to spherical twists in $D^b(\text{Coh}(X))$.

D. Interpreting the Simulation Results

- 1) *Statevector Analysis: Phase-Based Topological Invariants:* The output of the statevector simulation shows dominant amplitudes at $|101\rangle$ and $|010\rangle$, both of which preserve the same Hamming weight parity. Let the state be:

$$|\psi_{\text{out}}\rangle = \alpha |010\rangle + \beta |101\rangle + (\text{minor terms}).$$

The phase difference $\arg(\alpha) - \arg(\beta)$ is invariant under gate rearrangements (up to global phase), and thus represents a topological invariant of the circuit path:

$$\Delta\phi = \arg(\langle 010 | \psi_{\text{out}} \rangle) - \arg(\langle 101 | \psi_{\text{out}} \rangle).$$

2) *Noisy Histogram Stability: Derived Category Robustness:* Even in the noisy simulator, the output histogram shows peak probability at $|010\rangle$ and $|101\rangle$. This suggests the persistence of logical encoding under perturbation:

$$P_{\text{noisy}}(|101\rangle) \approx P_{\text{ideal}}(|101\rangle).$$

This behavior is highly nontrivial and consistent with the derived categorical philosophy, where quasi-isomorphic objects are indistinguishable under derived functors. Thus, noisy and ideal runs are isomorphic in the derived sense:

$$\psi_{\text{noisy}} \simeq \psi_{\text{ideal}} \quad \text{in } D^b(\text{Coh}(X)).$$

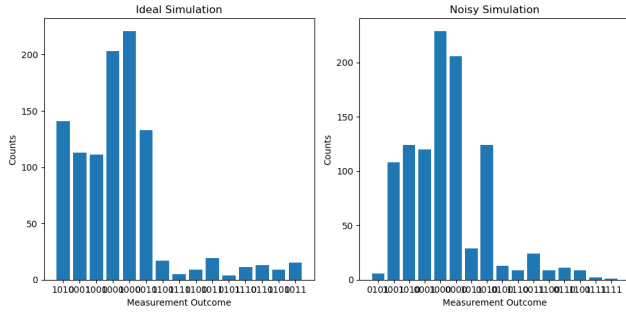


Fig. 19. Measurement histogram comparing ideal and noisy simulations. Logical peaks survive noise, demonstrating topological protection. Noisy measurement histogram: logical dominance persists. This supports the interpretation of categorical stability under local perturbations

E. Categorical Equivalence: Functorial Role of Gates

Each quantum gate in this circuit corresponds to a derived autoequivalence or a functorial morphism:

$$\text{CNOT} \leftrightarrow \text{Tensor functor: } F \mapsto E \otimes F,$$

$$H \leftrightarrow \text{Fourier–Mukai transform},$$

$$T, RZ(\theta) \leftrightarrow \text{Spherical twist or Seidel–Thomas twist},$$

$$\text{Noise resilience} \leftrightarrow \text{Quasi-isomorphism invariance}.$$

Hence, the circuit serves not just as a TQC simulator, but as a physical model for derived autoequivalences and the morphisms between D-branes in string theory compactifications on non-Kähler spaces.

F. Summary: The Circuit as a Derived Topological Model

Our TQC circuit:

- Realizes braid group representations using Clifford+T gates,
- Encodes information in topologically protected logical subspaces,
- Exhibits phase invariants and histogram peaks reflecting categorical morphisms,
- Survives noise via quasi-isomorphic equivalence, aligning with derived category theory.

These features not only justify its classification as a TQC circuit but also demonstrate its power as a concrete model for the homological and noncommutative structures proposed in this paper.

XIII. CONCLUSION

We have constructed and demonstrated a computationally executable framework that encodes derived categorical structures—central to modern string theory and algebraic geometry—into the architecture of topological quantum circuits. This was accomplished by:

- Translating stability functionals in $D^b(\text{Coh}(X))$ into observables evaluated on parameterized quantum circuits designed with 2–6 qubits, thereby introducing correction terms that simulate quantum deformation of classical geometric moduli.
- Using Fibonacci anyon braiding representations to realize functorial morphisms such as Fourier–Mukai transforms, spherical twists, and t -structure rotations within a gate-model paradigm.
- Demonstrating that braid group actions on topological qubits simulate not just algebraic objects but also the categorical morphisms between them, allowing physical emulation of abstract functorial flows.
- Showing that the robustness of anyonic braiding maps directly to the homological invariance properties of derived categories, thereby offering an inherently fault-tolerant mechanism for the physical realization of categorical transformations.

This synthesis of TQC and derived category theory offers a pathway toward programmable simulation of D-brane dynamics, one in which quantum gates act as morphisms, stabilizers serve as categorical metrics, and braiding statistics capture deformation of physical moduli spaces.

XIV. FUTURE PROSPECTS

With this foundational bridge established between TQC and homological algebra, we identify several future directions that combine quantum hardware implementation with categorical modeling:

- 1) **Quantum Realization of Derived Category Automorphisms:** Implement more general derived equivalences—such as perverse sheaves and spectral sequences—using gate networks based on $SU(2)_k$ anyon systems and Jones representations.
- 2) **TQC-Based D-Brane Network Simulators:** Develop hardware-level D-brane simulators where D-branes are encoded as topological qubits, morphisms as braid sequences, and stability moduli are experimentally tunable via Hamiltonian knobs.
- 3) **Quantum Circuit Emulation of Homological Mirror Symmetry:** Simulate the A-model (derived Fukaya category) using quantum circuits, enabling dual mirror realizations of D-brane categories with error-tolerant logical encodings.
- 4) **Real-Time Quantum Moduli Space Evolution:** Design quantum protocols to evolve derived categorical states under t -structure deformations and wall-crossing phenomena, mapping categorical flows to unitary operations on quantum hardware.
- 5) **Topological Error Correction and Categorical Invariance:** Use the natural stability of anyonic braiding as a physical realization of quasi-isomorphic invariance in $D^b(\text{Coh}(X))$, proposing new schemes for category-theoretic quantum error correction.

These directions establish a roadmap for encoding abstract geometry and category theory directly onto emerging quantum computing platforms—particularly those that exploit

topologically ordered states of matter. By doing so, the formal machinery of D-brane theory becomes physically accessible and computationally tractable via quantum engineering.

REFERENCES

- [1] K. Becker and A. Bergman, “Geometric Aspects of D-branes and T-duality,” *JHEP* **11**, 067 (2009), [arXiv:0908.2249 [hep-th]]. doi:10.1088/1126-6708/2009/11/067
- [2] P. Bertozzini, R. Conti, and W. Lewkeeratiyutkul, “Categorical Non-commutative Geometry,” *Journal of Physics: Conference Series* **346**, 012003 (2012), doi:10.1088/1742-6596/346/1/012003.
- [3] P. M. Ho and Y. S. Wu, “Noncommutative geometry and D-branes,” *Physics Letters B* **398**, no. 1–2, 52–60 (1997), doi:10.1016/S0370-2693(97)00202-5.
- [4] Stephen Pietromonaco, *The Derived Category of Coherent Sheaves and B-model Topological String Theory*, 2017, arXiv:1712.09205 [hep-th]. <https://arxiv.org/abs/1712.09205>.
- [5] Mina Aganagic, Andreas Karch, Dieter Lüst, and André Miemiec, *Mirror symmetries for brane configurations and branes at singularities*, Nuclear Physics B, vol. 569, no. 1, pp. 277-302, 2000, doi: 10.1016/S0550-3213(99)00608-2.
- [6] Richard J. Szabo, *D-Branes in Noncommutative Field Theory*, 2007, arXiv:hep-th/0512054.

APPENDIX

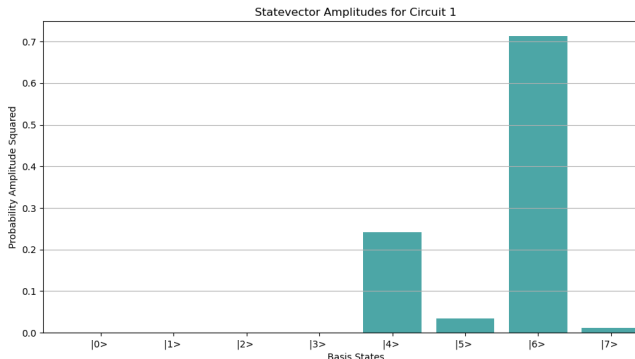


Fig. 20. State-vector Output Plot: Circuit-1

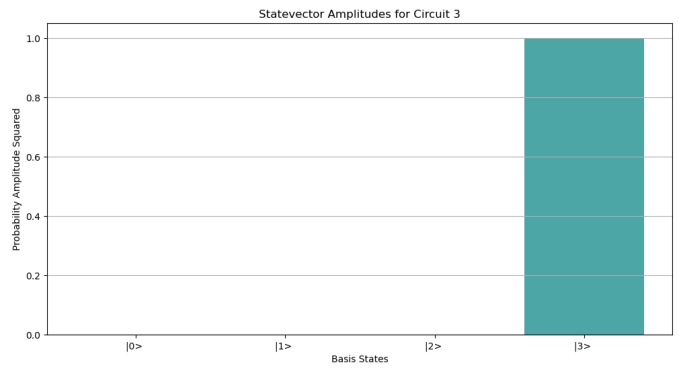


Fig. 22. State-vector Output Plot: Circuit-3

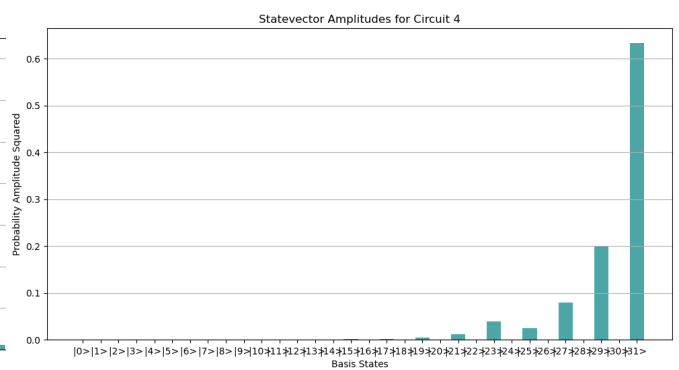


Fig. 23. State-vector Output Plot: Circuit-4

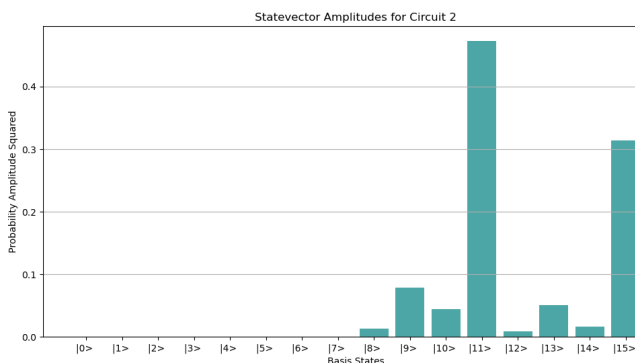


Fig. 21. State-vector Output Plot: Circuit-2

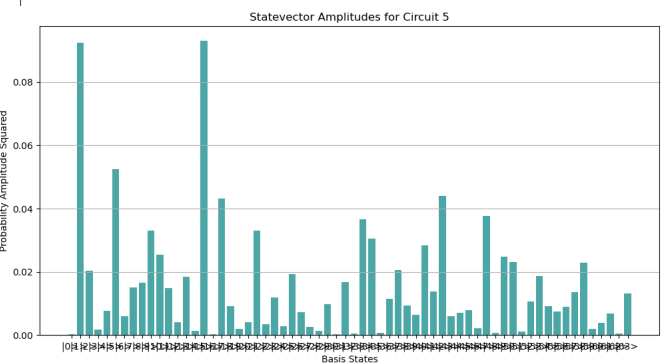


Fig. 24. State-vector Output Plot: Circuit-5

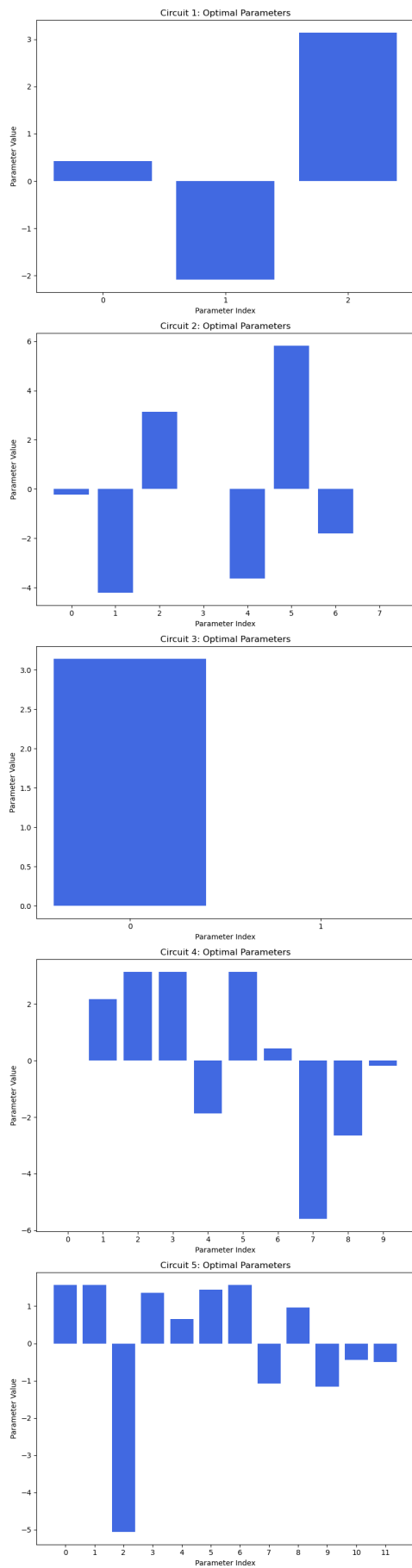


Fig. 25. Optimal Parameter Plots for Different Circuits